Nanoparticle Generation by Double- Pulse Laser Ablation

Emanuel Axente, Tatiana Itina, Jörg Hermann

Chapter 9

Nanoparticle generation by double pulse laser ablation

Emanuel AXENTE[1], Tatiana E. ITINA[2] and Jörg HERMANN[3]

[1]*National Institute for Lasers, Plasma and Radiation Physics, Lasers Department, "Laser-Surface-Plasma Interactions" Laboratory, PO Box MG-36, RO-77125, Bucharest-Magurele, Romania, e-mail: emanuel.axente@inflpr.ro*
[2]*Laboratoire Hubert Curien, CNRS 5516, Université de Lyon, 42000 Saint-Etienne, France, e-mail: tatiana.itina@univ-st-etienne.fr*
[3]*Laboratoire Lasers, Plasmas et Procédés Photoniques, LP3 CNRS – Aix-Marseille University, 13288 Marseille Cedex 9, France, e-mail: hermann@lp3.univ-mrs.fr*

The purpose of this chapter is to give a critical review of the processes involved in the generation of nanoparticles by material ablation with two time-delayed laser pulses. Experimental investigations of the ablation characteristics during nanoparticle synthesis with short double pulses are presented. In particular, the composition and the expansion dynamics of the ablated material are examined. The latest progress achieved in modeling laser-matter interactions in double pulse regime is discussed. The correlation between ablation efficiency and nanoparticle generation is assessed and compared with numerical simulations, the influence of interpulse delay on metals ablation being revealed.

9.1 INTRODUCTION

During de last decade, nanoparticles (NPs) have demonstrated huge potential for research and application in the fields of nanoscience and nanotechnology. Among them, noble metal-NPs have proven to be in the forefront of developments for sustained advances in fuel cells, analytical sensors, nanobiotechnology and nanomedicine due to their size-dependent electrical, optical, magnetic, and chemical properties [1-7]. Potential applications of noble metal-NPs in biomedicine are related, but not limited to: targeted delivery of drugs and other substances [8,9], chemical sensing and imaging applications [10,11], detection and control of micro-organisms [12], cancer cell photo-thermolysis [13,14]. This is first due to facile surface functionalization with specific biomolecules and second, to distinct optical properties related e.g. to localized surface plasmon resonance [3,4]. Wet chemical synthesis and functionalization of NPs are routinely used for obtaining a broad spectrum of nano-objects [4,5], from the "classical" colloidal gold nano-spheres, silver nano-rods, or silica/gold nano-shells, up to "exotic architectures" such as nano-cubes [15], nano-rice [16], nano-stars [17], or nano-cages [18]. Detailed information about the toxicological hazard of NPs was reviewed by Murphy *et al*. [5] and De Jong *et al*. [3].

Laser ablation (LA) is a unique tool for the fabrication of NPs, exhibiting several advantages over the classical wet chemical synthesis methods. On one hand, the main advantage of the LA technique is the possibility to preserve material stoichiometry during the ablation process [19]. On the other hand, LA is a faster and cleaner procedure since toxicity is difficult to avoid in traditional chemical routes of synthesis [20]. Indeed, NPs are directly generated during laser irradiation of bulk targets in vacuum, gas or liquid environments. Worth mentioning the high versatility of the method that allows the independent variation of the irradiation parameters like: laser wavelength, energy density, pulse duration, and repetition rate. As a consequence, a certain degree of freedom for tailoring NPs size and composition is possible while the fabrication of complicated nano-objects is a difficult task, most of NPs being spherical. Recent advances in laser synthesis of NPs with both nanosecond and femtosecond pulses are reviewed in the book chapters published by Besner and Meunier [21], Voloshko and Itina [19], and Caricato *et al*. [20]. Moreover, the processes involved in short pulse LA in vacuum and in a low pressure background gas, the generation of NPs and the deposition of NP-assembled films are discussed in Chapter 4 of this book.

Compared to nanosecond ablation, sub-picosecond laser-matter interaction is significantly different as illustrated in several experimental and theoretical studies [22-29]. It was shown that LA of metals with short laser pulses is an efficient tool to generate NPs having sizes in the range of a few nanometers [30,31]. Contrarily, in the nanosecond regime, the particles ejected directly from the target surface have significant larger sizes in the micrometer range [32], while smaller ones are formed by condensation during plume expansion. The difference in particle size is attributed to characteristic thermal regimes and thickness of the laser-heated layer [33,34] for the two irradiation cases.

Despite the large number of experimental studies reported in literature, the physicochemical mechanisms involved in NPs formation during LA are not yet fully understood. Two main approaches are currently applied for theoretical modeling of LA and NPs formation. Both are based on the two-temperature model considering that electrons and lattice have different temperatures under material excitation by short laser pulses [35]. The combination with a hydrodynamic model was employed in several numerical studies whereas the microscopic description using molecular dynamics was alternatively used in other numerical investigations. A large description of the theoretical models currently used in simulations, with their advantages and limitations was reviewed (see e.g. [19,20,36,37] and references therein). An improvement of the theoretical approaches requires therefore reliable experimental data for comparison.

A deeper understanding of short pulse LA and NPs generation from metal targets can be achieved from experiments using two time-delayed laser pulses. The so-called "*double pulse*" (DP) technique became popular, in particular in material analysis by laser-induced breakdown spectroscopy (LIBS), where an enhanced analytical signal and a better signal-to-noise ratio are beneficial [38,39]. Other experimental studies of DP-LA are related to investigations of plume dynamics [40], optimization of the nanoparticle size distribution in vacuum [41, 42] and liquids [43-47], probing electron-phonon coupling in metals [48] and modification of optical properties through ripples formation [49-52].

Modeling DP-LA with sub-picosecond laser pulses is a difficult task compared to the description of the single-pulse regime. Several competing physical processes should be considered in the case of LA with time-delayed pulses. These are: different laser absorption by the skin layer and in the subcritical plasma, electron thermodynamics, thermal conductivity, electron-phonon coupling, and the interaction of the pressure waves generated by time-delayed pulses [37]. Recent advances in the field of modeling short pulse laser-matter interactions can be found in the studies reported by Povarnitsyn *et al*. [37,53] and Roth *et al*. [54] and the references therein. Using a hybrid model that combines classical molecular dynamics and an energy equation for free electrons [37], the authors evidenced an elevation of the electron temperature in the plume up to three times when increasing the interpulse delay from 0 to 200 ps. The effect was accompanied by a monotonic decrease of the ablation crater depth, in agreement with experimental studies on aluminum and copper [37,53].

In this chapter, we give a critical review of short pulse LA of metals and NPs generation with two time-delayed femtosecond laser pulses. The next section is devoted to the description of typical experiments employed in DP laser-matter interactions. Both collinear and orthogonal irradiation geometries used for materials processing and analyses are explained, and representative results are presented for both cases. In the following, experimental results on DP-LA of metals (gold and copper) and NPs generation are presented and discussed with respect to the influence of the interpulse delay on plasma composition and crater depth. Examples from literature, covering other materials and experimental parameters are reviewed as well. The latest developments achieved in modeling laser-matter interactions in DP regime are presented in the last section.

Conclusions and perspectives of this fast-expanding research field are given at the end of the chapter.

9.2 TYPICAL EXPERIMENTAL DESIGN FOR LASER-MATTER INTERACTIONS WITH DOUBLE PULSES

The latest technological developments offer a high degree of freedom in controlling the laser pulse characteristics, including the temporal shape, the spatial distribution, the spectral profile, and the polarization state [55]. There are several approaches for DP excitation and ablation experiments. Usually, in most of the studies and in particular in the nanosecond regime, materials irradiation is performed using two laser sources synchronized by a delay generator, to trigger the pulse-to-target energy delivery and to control the interpulse delay [56]. A second approach refers to a Michelson interferometric setup, mostly in the femtosecond regime, in which the laser pulses emitted by a sole source are splitted into two beams. A delay line is interposed on one arm of the interferometer, the double pulses being generated after beam reconstruction [41,48,57]. Other recent concepts rely on programmable pulse shaping techniques, emphasizing ultrafast pulse tailoring in the spatio-temporal domain. They were described in details by Stoian *et al*. [55].

Double pulse laser-matter interaction is generally performed in two distinct configurations, with respect to the propagation direction of the pulses and their temporal sequence: the collinear and orthogonal geometries, as schematically depicted in Figures 1 and 2. A high experimental versatility is available for materials processing and analysis, several combinations being proposed in literature. Depending on the application, optimum energy delivery and subsequent material response can be achieved by the proper choice of the irradiation parameters. Accordingly, different beam geometries, pulse widths, wavelengths, interpulse delays, and pulse energies [38,58] are actively explored by the scientific community. Generally, the double pulse irradiation geometries are mostly used in material analyses by DP-LIBS, but also for the synthesis of thin films via pulsed laser deposition, and for nanoparticles generation in vacuum, gas or liquid environments.

9.2.1 Collinear double pulse interaction geometry

The collinear configuration, in which the two laser beams have the same propagation pathway, is the simplest but less versatile approach [58]. It is however the most used configuration, since it enables an easy alignment of the laser beams. For instance, it is mainly used in material analysis by DP-LIBS, combining different laser wavelengths (532/1064, 532/532, or 532/355 nm) as schematically depicted in Figures 1.a) and b). Consequently, improved sensitivity and lower detection limits were achieved for lead detection in metal alloys when LIBS was performed with an additional laser pulse [59]. The authors attributed the enhanced sensitivity to the higher plasma temperature.

Experiments of collinear double pulse laser ablation in liquid were carried out for studying the formation mechanisms of silver nanoparticles in water, and revealed the fundamental role of the cavitation bubble dynamics in the synthesis of aqueous colloidal dispersions [45].

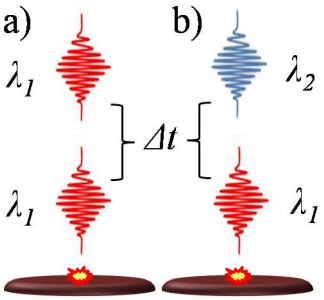

Figure 1. Scheme of double pulse ablation experiments in collinear geometry using one a) or two laser wavelengths b).

9.2.2 Orthogonal double pulse interaction geometry

In the orthogonal approach, one laser pulse ablates the sample (usually directed perpendicular to the surface) and the second pulse (propagating parallel to the sample surface) is applied either before, to form a pre-ablation spark, or after, in order to reheat the plasma generated by the first pulse [Figure 2.a)-c)]. Another possible arrangement is to irradiate the target at a specific angle (typically 45°) as schematically depicted in Figure 2.d). Although more complicated in terms of beam alignment, this experimental design is more versatile, and a broad range of pump-probe experiments are possible. Gautier *et al.* [60] demonstrated the intensity enhancement of emission lines ranging from a factor of 2 up to 100 during DP-LIBS analyses of aluminum alloys. The authors investigated the influence of interpulse delay and laser energy, and the physical mechanisms responsible for signal optimization. A comprehensive review on materials analyses by DP-LIBS, covering experimental studies, the fundamental mechanisms responsible for signal enhancement and applications, was published by Babushok and co-workers [38].

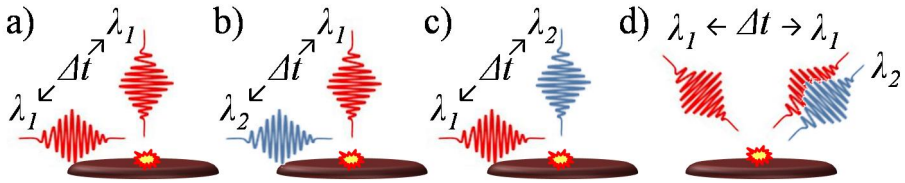

Figure 2. Orthogonal double pulse interaction geometries using a unique laser a), combining different wavelengths, energies and pulse durations b, c) for pre-pulse/re-heating mode, or at specific angles d).

9.2.3 Experiment for NPs generation with delayed short laser pulses

Although NPs formation in vacuum, gas or liquid environments is an intrinsic characteristic of short pulse laser ablation, studies demonstrated that the DP technique enables a better control of the NPs synthesis. A proper choice of the interpulse delay leads to the reduction of NPs and to an increased atomization of the ablation plumes [41]. Both effects are suitable for materials analyses by LIBS. Other possible applications are related to the deposition of ultra-smooth thin films by pulsed laser deposition [61] or for high-precision micromachining [62].

A schematic representation of the experimental setup used in the studies reviewed in this chapter is given in Figure 3. The ablation experiments were performed with a Ti:Sapphire laser source (λ = 800 nm, τ = 100 fs, f_{rep} = 1 kHz). A square aperture of 2 × 2 mm^2 was used to select the central part of the Gaussian beam that was imaged with an achromatic lens of 50 mm focal length onto the target surface. The two delayed laser pulses were obtained by turning the beam polarization, passing through a half-wave plate, and splitting the beam with the aid of a polarized large band prism.

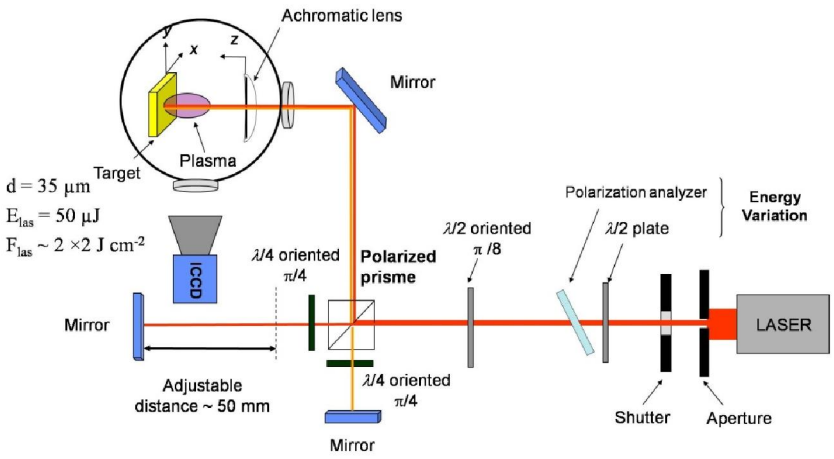

Figure 3. Schematic representation of the experimental setup.

Each beam crosses a quarter-wave plate before and after reflection on a mirror at 90° incidence. After recombination by the prism, two laser pulses of equal energy and orthogonal polarization were obtained. The interpulse delay was varied from 0 to 300 ps by adjusting the length of one beam path. According to the total laser pulse energy of 2 × 25 μJ incident onto the sample surface and a spot diameter of 35 μm, a maximum laser fluence of 2 × 2 J cm^{-2} was available. A mechanical shutter was used to control the number of applied double pulses.

The metal targets were placed in a vacuum chamber of 10^{-4} Pa residual pressure. Inside the chamber (Figure 4), the target holder and the focusing lens were mounted on motorized translation axes. A glass plate placed between target and lens prevented the latter to be coated by the ablated material. The glass plate was replaced regularly to minimize the laser beam extinction by the deposit. Fast plume imaging was performed with the aid of a focusing objective

and an intensified charge-coupled device, orthogonal to the symmetry axis of plasma expansion (see Figure 3). The delay between laser pulse and observation gate was set to 400 ns with the aid of a delayed pulse generator. During the experiments, 20 laser shots were applied at maximum to each irradiation site to avoid deep crater drilling and to keep the ablation process and plume dynamics reproducible.

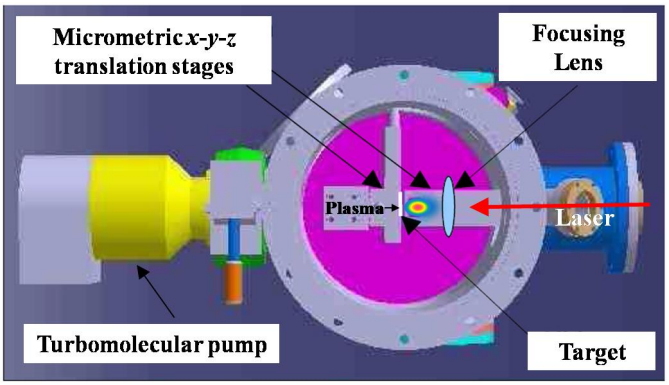

Figure 4. Up-side view of the reaction chamber used in the collinear ablation geometry.

For measurements that require data acquisition over more than 20 ablation events, several sites were irradiated by translating the target by 50 μm perpendicularly to the laser beam propagation. The laser-produced craters were investigated by optical microscopy after the ablation experiments. The ablated material was collected on mica substrates, placed parallel to the target at a separation distance of 20 mm from the target surface. Atomic force microscopy operated in tapping mode was used to analyze the obtained NPs. Several areas of 2×2 μm^2 were scanned to characterize each sample in order to count a number of particles sufficiently large for statistical analysis of the particle size distribution.

9.3 INVESTIVATION OF NANOPARTICLES PRODUCED BY SHORT DOUBLE PULSE LASER ABLATION OF METALS

Several experimental and theoretical studies devoted to short pulse laser ablation evidenced that nanometer-sized particles represent a large fraction of the ablated material [25,63-67]. This characteristic feature of short pulse LA is attributed to the fast heating and energy relaxation. Two principal mechanisms of NPs generation during the quasi-adiabatic plume expansion were proposed [68,69]. The first one called *"phase explosion"* or *"thermal decomposition"* [70,71] consists in the transformation of matter into a liquid-gas mixture that favors the NPs generation. The second - *"mechanical decomposition"* of the metastable melt due to shock- and rarefaction waves is considered another source of efficient NPs generation [72]. The influence of pressure relaxation on LA physical processes was addressed by Chimier *et al*. [69] and Norman *et al.* [73]. Contrary to the

nanosecond regime, NPs formation by condensation is supposed to play a minor role in case of short pulse LA under vacuum [22].

In the present section, we evaluate the influence of the interpulse delay on the composition of the laser-produced plasma and on the quantity of ablated copper and gold targets. To this purpose, a brief summary of the mechanisms involved in single pulse metals ablation and NPs generation during intense short pulse laser irradiation is first presented in the next section.

9.3.1 Correlation between ablation efficiency and nanoparticle generation in single pulse regime

Experimental investigations, correlating the properties of the plume with measurements of the laser-produced crater volumes, allowed us to evidence two distinct ablation regimes for copper and gold that were also observed for other metals [74-76]. The two regimes are related to the applied laser fluence (F_{las}) and strongly coupled with the plume composition [25].

In the "*low-fluence*" regime, a small increase in ablation depth with F_{las} is observed, and a large fraction of the ablated material is atomized. The "*high-fluence*" regime is characterized by the efficient NPs generation. As the ejection of clusters occurs when the absorbed energy density is smaller than the one required for complete metals atomization, the ablation efficiency increases with the amount of NPs within the plume [25].

Comparing the single pulse LA of copper and gold, three main conclusions could be highlighted (see Figure 5): (i) the transition fluence characteristic to each ablation regimes is higher in case of copper, (ii) both the ablation rate and efficiency are smaller for copper, and (iii) the relative fraction of NPs within the plume is smaller for copper.

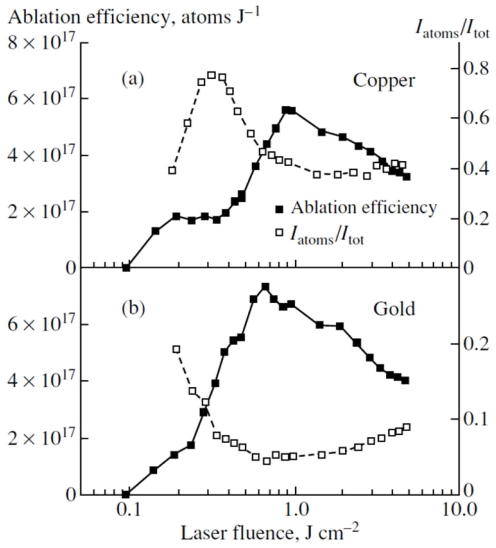

Figure 5.Ablation efficiency and atomization degree of copper (a) and gold (b) as functions of F_{las} [25].

These differences are attributed to the different heat regimes of the two metals. Compared to gold, copper has a much larger electron-lattice coupling and the energy transported towards the bulk via fast electron heat diffusion is lower and characterized by a smaller depth. Consequently, a steeper temperature depth profile and a thinner heat-affected zone are expected for copper. According to the larger energy density deposited in a thinner layer, the observed plume atomization is higher. Contrarily, the thicker melted zone in case of gold favors the NPs generation. Since the thickness of the melted surface layer increases with F_{las} faster for gold, the onset of efficient NPs generation occurs at a lower fluence for the precious metal.

9.3.2 Influence of interpulse delay on plume composition

It was shown in the previous studies that the NPs fraction generated during metal ablation only weakly depends on the laser fluence [64], but is strongly influenced by the strength of electron-lattice coupling [25]. This behavior was attributed to the competition between the fast electron heat transport and the energy transfer to the lattice that governs the metals heat regime for irradiation with laser pulses shorter than the characteristic time of electron-lattice thermalization τ_{el}.

The results presented here were obtained with collinear double pulses following the experimental procedure described in *Section 9.2.3*. Two plume images, recorded during single pulse LA of copper with F_{las}= 4 J cm^{-2} a) and with two time-delayed laser pulses of 2 J cm^{-2} delayed by 33 ps b), are shown in Figure 6. The delay between observation gate and laser pulses was 400 ns. In both images, two distinct plume components are observed. A "slow" component of high emission intensity is located close to the target surface whereas a "fast" component, of lower intensity, is observed at larger distance. The splitting into two main velocity populations in the plasma expansion was observed for short pulse LA of several metals [22,24,64]. Combined analysis by time-resolved imaging and optical emission spectroscopy revealed that the fast component contains neutral atoms mainly, whereas NPs dominate the slow one [25,64,77]. In the images below, the ten-level color palette is adjusted to the emission intensity of NPs.

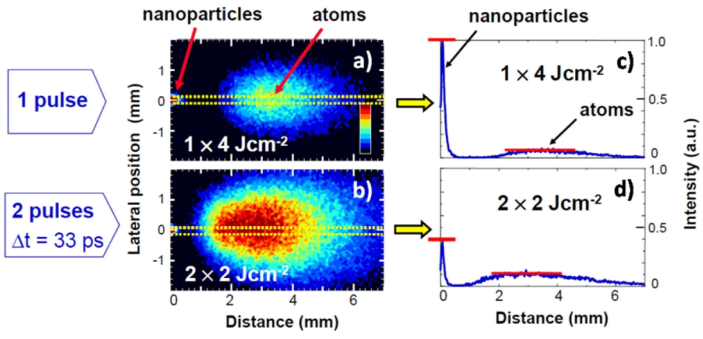

Figure 6. Plume images recorded during single pulse LA of copper a) and with two pulses delayed by 33 ps b). The intensity profiles c) and d) were obtained from the images a) and b), respectively.

With respect to the single pulse experiment, Figure 6.a), a large increase of the emission intensity of the atomized plume component is observed when two delayed pulses were applied b). In the same time, the NPs plume intensity decreases as revealed by the intensity profiles presented in Figures 6.c) and d). The profiles were obtained from the plume images a) and b), by averaging the signal intensity over several pixel rows along the plasma symmetry axis [see the yellow dashed lines in Figures 6.a) and b)]. Moreover, it is shown that the maximum intensity position of the atomized plume component is shifted towards the target surface for the DP case. This behavior may be due to the interaction of the second pulse with the expanding plasma.

The emission intensities of atoms and NPs deduced from the plume images are presented in Figure 7 as functions of interpulse delay for copper a) and gold b). Strong changes of the plume composition occur for both metals with increasing interpulse delay. Indeed, the emission intensity of atoms increases by a factor of four whereas the NPs intensity decreases by the same amount. Moreover, the intensity changes occur at a shorter delay for DP-LA of copper a), with respect to ablation of gold b). The black lines in Figure 7 present the intensity increase and decrease according to formula (1) below, suggesting thus different characteristic times for the observed plume composition changes.

The evolution of the emission intensity changes of both components versus interpulse delay Δt was described using the following biexponential function [41,78]:

$$I(t) = I_0 + I_1\left(1 - e^{-\Delta t/\tau_1}\right) + I_2\left(1 - e^{-\Delta t/\tau_2}\right). \quad (1)$$

Here, I_0 is the intensity for an interpulse delay at Δt = 0, I_1 and I_2 are the amplitudes of intensity changes that occur on different time scales, characterized by τ_1 and τ_2, respectively. The continuous and dashed lines represent the emission intensities of atoms and NPs, respectively, calculated with formula (1) using the parameters listed in Table 1.

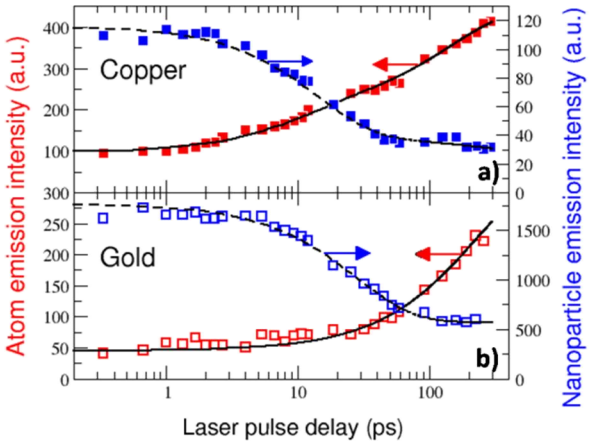

Figure 7. Emission intensities of atoms (red squares) and NPs (blue squares) deduced from plume images (see Figure 6) vs interpulse delay for two laser pulses of 2 J cm^{-2} [78].

Table 1. Intensity values I_0, I_1 and I_2 and characteristic times τ_1 and τ_2 used to describe the emission intensity evolution of atoms and NPs as functions of interpulse delay using the biexponential function (1).

Metal	Plume component	I_0 (a.u.)	I_1 (a.u.)	I_2 (a.u.)	τ_1 (ps)	τ_2 (ps)
Cu	atoms	95	105	240	10	140
Cu	NPs	117	-78	-12	13	200
Au	atoms	45	0	240	-	200
Au	NPs	1740	-1170	0	30	-

The approximation by a biexponential function revealed two characteristic times for the observed plume compositional changes. The shorter time τ_1 was deduced to be about 10 ps for copper and 30 ps for gold. In good agreement with other studies [79,80], these values are close to the characteristic times of electron-lattice relaxation $\tau_{el} \approx 1–10$ ps and 30–100 ps for copper and gold, respectively. The second parameter τ_2 was found about one order of magnitude larger than τ_1. It was suggested that it characterizes a slower process, strongly influencing the atomic emission intensity increase as revealed by the relative large amplitude deduced (see I_2 value in Table 1). The slow process has a negligible influence on the NPs plume component as illustrated by intensity ratio $I_2 / I_1 << 1$.

The physical mechanisms involved in the modification of plume composition with increasing interpulse delay were explained by Noël and Hermann [41]. First, according to the two-temperature model [35], during short-pulse LA the material properties depend on both electron and lattice temperatures, T_e and T_l respectively. Thus, the electron heat conductivity k_e diminishes with the T_l, as predicted by the simplified expression $k_e \approx T_e/T_l$ proposed by Kanavin *et al.* [81] for small T_e. Consequently, for delays $\Delta t \approx \tau_{el}$ the energy deposited by the second laser pulse is confined in a small volume since T_l is large and thus k_e is small at this stage and the energy transport towards the bulk reduced. The increased energy density promotes the growth of the atomization degree within the ablation plume. Second, for larger interpulse delays, the atomized plume component is heated up by inverse bremsstrahlung, leading thus to an enhanced atomic emission intensity, as also reported by several authors [57,82]. Indeed, complementary analyses by optical emission spectroscopy [78] evidenced the increase of plume temperature and ionization degree. The observation of plume temperature increase was also confirmed by modeling [37]. Moreover, an amplification of both mechanisms could be foreseen by the interaction of the second laser pulse with hot clusters and bubbles that start growing at times of the order of τ_{el} [41].

The decrease of the NPs fraction with increasing interpulse delay was further confirmed by atomic force microscopy (AFM) analyses of the ablated material collected on mica substrates [41]. To demonstrate the strong decrease of NPs number with Δt, we present in Figure 8 AFM images of mica substrates after deposition with 500 laser double pulses and different interpulse delays. With respect to ablation with Δt = 0 a), the number of NPs is strongly reduced when increasing the interpulse delay to 6 ps b). A further decrease was evidenced for longer Δt-values as illustrated in Figure 8c), where only a few, smaller NPs are observed.

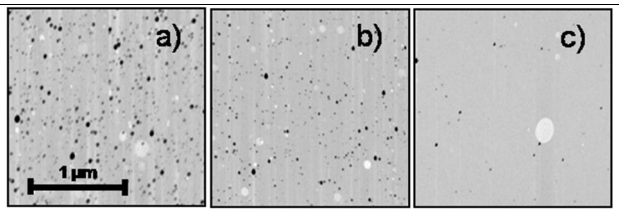

Figure 8. AFM images of copper NPs collected on mica substrates during ablation with two laser pulses of 2 J cm^{-2}, delayed by 0, 6 and 90 ps, respectively for a), b) and c) [78].

9.3.3 Influence of interpulse delay on ablation depth and crater morphology

The ablation depth was measured in the following way: for each interpulse delay, series of 10 craters were drilled with an increasing number of applied double pulses, as shown in Figure 9. The depth of each crater was measured using optical microscopy by focusing on the samples surface and the crater bottom [83]. According to the linear increase of crater depth z with the number of double pulses n_{las}, the ablation depth was deduced from the slope $\Delta z/\Delta n_{las}$.

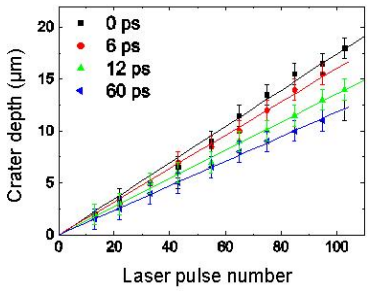

Figure 9. Crater depth vs number of applied double pulses for ablation of copper with various interpulse delays. The ablation depth (per double pulse) was deduced from the slope [78].

The ablation depth as a function of interpulse delay is presented in Figure 10 for DP-LA of copper and gold. For an interpulse delay $\Delta t = 0$, the ablation depth equals the value obtained with a single pulse of F_{las} = 4 J cm^{-2}, whereas the depth measured for large delays is slightly smaller than the value observed for a single pulse of 2 J cm^{-2} fluence. The number of NPs deduced from the AFM analysis is presented in Figure 10 as a function of interpulse delay and compared to the biexponential function [equation (1)] that was previously used to characterize the NPs emission intensity during copper ablation (see Figure 7). Similar to the characterization of the plume emission intensities, we approximate the ablation depth by a biexponential function, replacing the intensity values in equation (1) by the appropriate depths (continuous and dashed lines for copper and gold, respectively). It is noted, that the times τ_1 and τ_2 equal the characteristic times of the plume intensity evolution. The main contribution of the observed ablation depth decrease is attributed to the change of the samples heat regime as we have

$z_1 >> z_2$, similar to the evolution of NPs emission intensity. This confirms that NPs present the major part of the ablated mass.

This behavior is in agreement with the ablation depth measurements performed by Semerok and Dutouquet [57] after laser ablation of aluminum and copper with short laser pulses of durations ranging from 50 fs to 2 ps. The authors reported that the craters obtained in the DP regime were almost two times deeper for Δt < 1 ps. For interpulse delays in the 1–10 ps range, the crater depth decreased with increasing interpulse delay. Finally, for $\Delta t \geq 10$ ps, the crater depth obtained with double pulses equaled the depth drilled with a single pulse [57]. Moreover, the authors observed that, compared to single pulse ablation, the use of double pulses of equal total energy leads to a 10 times higher plasma emission intensity, if interpulse delays in the range from 100 to 235 ps were applied.

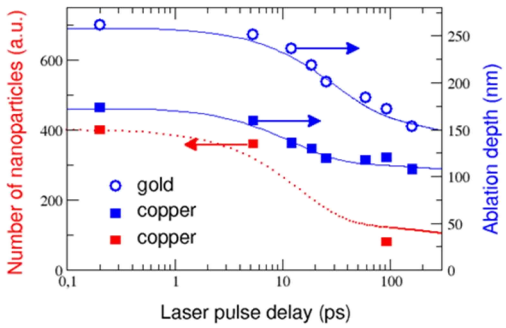

Figure 10. Number of Cu NPs (red color) deposited on mica substrates with double pulses of 2 × 2 J cm^{-2}. The decrease vs interpulse delay is similar to that of the NPs emission intensity presented by the dotted line (taken from Figure 7). The ablation depths of Cu (squares) and Au (circles) are also shown. The continuous and dashed lines were obtained using equation (1) for τ_1 = 12 and 30 ps, respectively, replacing the characteristic intensities by the appropriate depths [78].

The hybrid molecular dynamics - two-temperature model developed by Povarnitsyn *et al*. [37] confirms the measured crater depth evolution as a function of interpulse delay. It is concluded that the crater depth reduction is related to the formation of a high-pressure zone inside the plume. This suppresses the fragmentation in the rarefaction wave caused by the first pulse for $\Delta t \leq 20$ ps, and merges the inner ablated layers of atoms with the target surface for delays ≥ 50 ps [37].

Although less investigated, the morphology of the craters drilled by DP in a material is also influenced by the interpulse delay. In the single pulse regime, the best surface microprocessing results are usually obtained by applying low laser fluencies, close to the ablation threshold. Le Harzic *et al*. [84] investigated DP laser-processing of metals (steel, Al and Cu) in order to get insights in materials microstructuring when a high speed - high fluence regime is required. The authors evidenced a significant quality improvement in metal microstructuring (less removed or recast matter) via DP-LA. For interpulse delays typically smaller than 1 ps, the structures formed in the crater bottoms are less

pronounced when double pulses were applied. They exhibit fewer spikes or pit craters, while the surface seems to be smoother.

Short double pulses of 180 fs duration and equal intensity, separated by an interpulse delay from a few hundred fs to 22 ps, were used by Spyridaki *et al*. [85] to irradiate silicon targets in vacuum. The authors found that for $\Delta t > 3$ ps, the second pulse couples efficiently to the liquid layer formed at the surface, leading to the total vaporization of the melt. As a result, a featureless structure without a residual cast is generated onto the silicon surface, in contrast to the single pulse regime that produces significant thermal and hydrodynamic effects in the residual melt [85].

An improvement of the crater morphology was reported by Stoian *et al*. [86] in case of short pulse LA of dielectrics using temporally shaped pulse trains with sub-picosecond separation. Cleaner structures with lower stress were thus obtained by the sequential energy delivery to the targets.

9.3.4 Overview of other investigations in the field of double pulse laser-matter interactions

Experimental results obtained by DP-LA were reported in several studies, generally revealing similar observations. Semerok and Dutouquet [57] investigated the characteristics of LA and plasma re-heating with ultrashort DP of 50 fs and 10 ps durations, time-delayed from 50 fs up to 250 ps. The authors studied the influence of the interpulse delay on the ablation features (efficiency, crater diameter, depth, volume and shape) and on the laser plasma properties (shape and dimensions, expansion velocity, intensity and lifetime, pulse-to-pulse reproducibility) on aluminum and copper targets. They observed an increase of plume brightness and a decrease of crater depth for delays ranging from of 1 to 10 ps. Both effects were attributed to partial plasma shielding, while 100–200 ps delay was determined as optimum for plasma re-heating by the second pulse. During DP-LA on the same metals, Le Harzic *et al.* [84] observed a reduced ablation depth and a smoother crater bottom when applying a second laser pulse with $\Delta t < 1$ ps. Scuderi *et al.* [82] performed plasma analyses via time-resolved optical emission spectroscopy during DP-LA of titanium with pulses of 100 fs duration. The authors observed that the amount of NPs decreased with the interpulse delay, whereas the number of atoms and ions increased. The changes of plume composition were attributed to NPs fragmentation. Moreover, they claimed the possibility to tailor plume components over different characteristics such as the kinetic energy of ions and neutrals, their relative fraction, and over the NPs production efficiency. Results on DP-LA of nickel in vacuum using pulses of 250 fs duration delayed by 1–1000 ps were reported by Donnelly *et al*. [40]. The authors observed that the increase of the interpulse delay from 10 to 100 ps provoked a decrease of the crater volume by more than a factor of 2 (up to a value below the single pulse regime), while the ion yield was strongly enhanced. They attributed this behavior to the interaction of the second laser pulse with the material ablated by the first pulse. The evolution of NPs ejected during short pulse LA (250 fs) of certified copper-based alloys and relative calibration plots of a fs–ns DP-LIBS orthogonal configuration was investigated by Guarnaccio *et al*. [87]. The authors stated that their particular DP-LIBS configuration can provide

new perspectives for compositional analyses of materials. Recently, Garrelie *et al*. [88] investigated the effects of temporal laser pulse shaping during LA of aluminum and graphite targets in the view of optimizing thin films synthesis by femtosecond pulsed laser deposition. *In situ* optical diagnostic methods were used to monitor the expansion and the excitation degree of atomic species and NPs. The authors showed that the use of optimized pulse shapes leads to a decreased NPs production by balancing the thermo-mechanical energy content. Short DP-LA (pulses of 100 fs separated by delays up to 90 ps) during drilling of aluminum and copper films was studied by Wang *et al*. [89]. The authors reported that the drilling efficiency in DP regime is not higher compared to single pulse drilling with the same total energy. The size of NPs re-deposited around the drilled craters was found to depend on the metal (having different electron–phonon coupling parameters). In addition, the particle size was shown to decrease with increasing interpulse delay. The authors concluded that the drilling process can be regulated by varying the interpulse delay, and an even more efficient processing control is possible by using a shaped femtosecond laser pulse train [89].

Several studies were also devoted to DP-LA of semiconductors and dielectrics [85,90-93]. Analyses by time-of-flight mass spectrometry [85] and optical emission spectroscopy [92,93] were performed during DP-LA of silicon, demonstrating that the ion yield and the plume emission intensity significantly increase with the interpulse delay in the range of some tens of picoseconds. Moreover, the laser-produced crater seemed smoother [85]. These changes were attributed to alterations of the optical properties when the material reaches the melted state. With respect to solid silicon, the melt exhibits a decreased optical penetration depth, leading thus to an increased laser energy coupling. The optical breakdown thresholds in silica and silicon were measured using DP of 40 fs duration by Deng *et al*. [91]. By varying laser energy and interpulse delay, they found that the total energy required for breakdown decreases for silica and increases for silicon with the elevation of the first pulse energy. Chowdhury *et al*. [90], conducted pump-probe experiments on femtosecond DP-LA of fused silica by investigating the plasma dynamics versus interpulse delays. They found that the total ablated volume decreased with increasing interpulse delay and attributed the lowering to the screening by the plasma generated by the first pulse [90]. Stoian *et al*. [86] demonstrated an improvement in the quality of femtosecond laser microstructuring of dielectrics by using temporally shaped pulse trains [55].

With respect to NPs synthesis by conventional wet chemical procedures, short pulse LA of metals in liquids exhibits several promising advantages such as environmental sustainability, simple experimental set-up, and long-term stability [44,45,94,95]. Compared to NPs generation in vacuum and/or low pressure gas backgrounds (see Chapter 4 for details), LA in liquids evidenced the possibility to fabricate nanomaterials with special morphologies, microstructures and phases, and to design various functionalized nanostructures in a single-step process, as reviewed by Zeng *et al*. [44]. The physical mechanisms of NPs formation by single pulse LA of metals in liquid environment were recently addressed by Povarnitsyn *et al*. [28].

Besner *et al*. [96] proposed a laser-based method to control the size characteristics of gold colloidal NPs by the generation of femtosecond laser-

induced supercontinuum. Highly stable aluminum NPs generated via single pulse LA in ethanol using either femtosecond (200 fs) or picosecond (30 and 150 ps) laser pulses were obtained by Stratakis *et al*. [97]. An exhaustive description of NPs synthesis by single pulse LA in liquid environments can be found in [98]. However, DP-LA attracted less interest and DP experiments in liquids were performed mostly in the nanosecond regime in view of analytical purposes.

Burakov *et al*. [99] reported that metal ablation by double pulses in transparent liquids could lead to the fabrication of stable, size-selected NPs, with an increased production efficiency. Silver NPs colloidal solutions were obtained by Phuoc *et al*. [100] using DP-LA in the orthogonal configuration, with the goal of inducing fragmentation for an improved NP size control. Experiments performed in collinear geometry for production of metal (Ag, Au, Cu) NPs revealed an enhanced synthesis rate and an increased emission signal from the plasma atoms and ions due to more efficient material ablation [101]. Titanium DP irradiation under water has been investigated both theoretically and experimentally by Casavola *et al.* [102]. The authors evidenced that the dynamics of the plasma is strongly affected by chemical reactions between plume species and vaporized liquid within the laser-induced cavitation bubble. Later, the same group reported on collinear DP-LA in water for the synthesis of silver NPs [45]. Several optical and spectroscopic techniques were employed to study the dynamics of laser-induced plasma and cavitation bubbles, and to monitor Ag NPs generation as a function of interpulse delay. They concluded that: (i) smaller NPs were produced at interpulse delays corresponding to the early expansion and late collapse stages of the cavitation bubble; (ii) higher nanoparticle concentrations were obtained with DP-LA when the interpulse delay matches the maximum volume of bubble expansion [45].

As mentioned before, double pulse laser irradiation was also applied for thin films synthesis by pulsed laser deposition. However, in most of the studies, two targets are simultaneously ablated by two synchronized laser pulses, in order to obtain doped thin films or multilayered structures. Typically, UV excimer lasers operated at either 193 or 248 nm are used in combination with Q-switched Nd:YAG lasers operated at 355 or 532 nm to grow ferromagnetic NiMnSb [103], Al doped ZnO [104], Au doped TiO_2 [105,106], and Au doped NiO thin films [107]. Double pulses were also used in reactive pulsed laser deposition where an improved quality of deposited carbon nitride films was obtained for an optimized interpulse delay [108].

Despite the success in obtaining stoichiometric thin films, pulsed laser deposition is often affected by the presence of micrometer-sized droplets that may lower the coatings quality in certain applications. György *et al.* [109] investigated the morphology of the Ta thin films obtained by double pulse laser irradiation. In their experiments, an UV laser beam (λ = 193 nm, $\tau_{FWHM} \approx 10$ ns) was used for material ablation, and a delayed IR laser (λ = 1.064 μm, $\tau_{FWHM} \approx 10$ ns), propagating parallel with the target surface, was used for the interaction with the particulates present in the ablation plume. The authors analyzed the density of particulates on the surface of the films as a function of the delay between the UV and IR laser pulses and evidenced the possibility of obtaining particle-free Ta thin films.

9.4 MODELING OF DOUBLE PULSE LASER ABLATION

9.4.1 Fundamentals of laser-matter interactions

In the case of nanosecond laser ablation, the most common and simplest model that describes laser-solid interaction is based on a "*thermal effect*" [110]. The problem of evaporation of a metal surface heated up to a certain temperature T_0 was considered by a number of authors, for example, by Anisimov *et al.* [111]. The equilibrium evaporation law may be then obtained by using the well-known Hertz-Knudsen equation. However, laser ablation often occurs under non-equilibrium conditions. Therefore, several groups considered non-equilibrium surface processes [112]. In particular, the role of a so-called "*phase explosion*" mechanism was discussed [113,114,115]. In addition, photo-physical ablation of organic polymer materials was examined [116].

Recently, femtosecond laser systems attracted particular attention [27,71,117-119]. Several theoretical investigations have already underlined the main physical processes involved in the ultra-short laser-matter interactions [34,120-122]. The classical approach is based on the two-temperature model [35]. In addition, several hydrodynamic simulations were carried out to describe the target material motion [123-125]. In particular, shock wave propagation was shown to play a crucial role in these calculations. Molecular dynamics simulations were furthermore performed to provide even more detailed insights into the laser ablation mechanisms, such as phase explosion, fragmentation, evaporation, and mechanical spallation [80,126,127].

A typical hydrodynamic model is based on the solution of a system of either Lagrangian [128] or Eulerian hydrodynamics [129]. These equations were extended to the case of two-temperature hydrodynamics and supplemented by a laser energy absorption source, electron heat conductivity and electron-phonon energy exchange terms [130]. To complete the model, a properly chosen equation of state (EOS) should be used. Previously, a semi-empirical thermodynamically complete EOS with separated components of electrons and lattice (heavy particles) was used for metals, such as aluminum [131]. This EOS is developed to fulfill the following requirements: (i) to describe experimental results on compression and expansion for a wide range of densities and temperatures including data on critical and triple points; (ii) to contain separate information about electron and ion/lattice sub-systems; (iii) to represent changes of thermodynamic parameters during phase transitions. Here, we switched between two different modifications of the EOS: (i) with metastable states; and (ii) without metastable states.

To account for the kinetic processes, an estimation of a lifetime was introduced for the superheated liquid (metastable state). Thus, when the binodal line is crossed [27], a particular treatment was applied to each of the following two competitive effects: (i) for the spinodal decomposition, a criterion of the metastable liquid lifetime, based on the theory of homogeneous nucleation [132] is used; (ii) for the fragmentation, a mechanical failure algorithm of Grady [133] is applied. In the first case, we estimated the lifetime of the metastable liquid as $\tau = (CnV)^{-1}e^{(W/k_BT)}$, where $C = 10^{10}$ s^{-1} is the kinetic coefficient, n is the concentration, V is the volume, $W = 16\pi\sigma^3/3\Delta P^2$ is the work needed to cause the phase transition, ΔP is the difference between saturated vapor pressure at the

same temperature and the pressure of substance, k_B is the Boltzmann constant, and T is the temperature of the sub-system of heavy particles. The temperature dependence of the surface tension is described as $\sigma = \sigma_0(1 - T/T_c)^{1.25}$, where T_c is the temperature in the critical point, and σ_0 is the surface tension at normal conditions. In this case, as soon as the lifetime τ in the volume V is expired, the phase state in this point is no more metastable. The EOS with metastable phase states is therefore no more relevant in this volume, so that the corresponding thermodynamic properties should be rather calculated by using the stable EOS. To account for the second effect, a fragmentation criterion was used for the liquid phase with the spall strength $P_s = (6\rho^2 c^3 \sigma\dot{\varepsilon})^{1/3}$and the time required for fragmentation $t_s = {}^{1}/_{C}\,(6\sigma/\rho\dot{\varepsilon}^2)^{1/3}$, where ρ is the density, $\dot{\varepsilon}$ is the strain rate, and c is the sound speed. When this criterion was satisfied, we introduced vacuum into the cell and relax the pressure to zero. Both of these criteria are used simultaneously and each of them can prevail in a given computational cell depending on the substance location on the phase diagram.

Laser energy absorption by the conduction band or free electrons is described by solving the following system of Helmholtz equations:

$$\frac{\partial^2 E}{\partial z^2} + k_0^2[\varepsilon(z) - \sin^2\theta_0]E = 0, \quad (2)$$

$$\frac{\partial^2 B}{\partial z^2} + k_0^2[\varepsilon(z) - \sin^2\theta_0]B - \frac{\partial ln\varepsilon(z)}{\partial z}\frac{\partial B}{\partial z} = 0, \quad (3)$$

where $E(z,t)$ and $B(z,t)$ are the slowly varying laser field amplitudes; $\varepsilon(z,t)$ is dielectric function calculated for the given layer at a given time; and θ_0 is the angle of incidence. Equations (2-3) are solved by using a transfer-matrix method [134] for both s and p polarizations. The absorbed laser energy can be then calculated as follows:

$$Q_L(t,z) = \frac{\omega}{8\pi} Im\{\varepsilon(z,t)\}|E(t,z)|^2. \quad (4)$$

Molecular dynamics (MD) simulations coupled to a two-temperature model (TTM) can be used as an alternative to such two-temperature hydrodynamic methods [37,122]. In the MD-TTM method, the dynamics of the atomic subsystem is determined by an interatomic potential and boundary conditions. For metals, an embedded atom model [135] is often used. It accounts for both a pair-wise interaction and a contribution of the electron charge density from nearest neighbors of an atom under consideration.

9.4.2 Numerical simulations of short double pulse interaction with materials

Double pulse experiments are first studied with the aid of recently developed MD-TTM model [37]. Here, the target free surface is placed at z = 0 nm and the laser beam propagates in the positive direction of z. The ablation dynamics is analyzed by using contour plots of the main thermodynamic parameters for different delays between the laser pulses. When Δt = 0, the dynamics of ablation corresponds to the case of a single pulse with the doubled incident fluence. At delays up to 20 ps, the target expansion sets in, resulting in the enlargement of the absorption region.

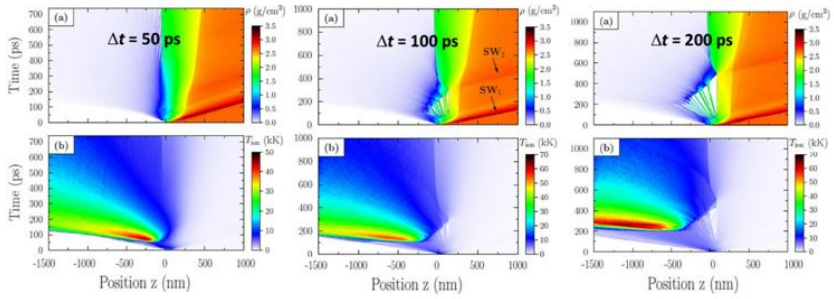

Figure 11. Contour plots of the density a), temperature of ions b) for different interpulse delays: left - 50 ps; middle - 100 ps; and right - 200 ps [37].

For longer delays, shielding of the target surface by the nascent plume enters in the play. At a delay $\Delta t \approx 50$ ps (Figure 11, left) a rarefaction wave produced by the first laser pulse passes through the melted surface layer, leading to its fragmentation. The plasma temperature is as high as 50000 K in the zone of absorption of the second laser pulse. In this case, the second shock wave with an amplitude of about 2 GPa starts its motion from the plume region towards the bulk. This wave is followed by the second rarefaction wave. Its power is, however, insufficient to cause spallation of the liquid layer [37].

For the delay of 100 ps (Figure 11, middle), the second pulse energy absorption is observed at $z \approx -500$ nm, while the plume temperature reaches about 70000 K. The power of the second shock wave is sufficient to completely eliminate the fragmentation produced by the first pulse by erasing the created voids. As the absorption of the second pulse takes place far enough from the initial surface of the target (in the leading edge of the nascent ablation plume), the collapse of voids is finished by $\Delta t \approx 350$ ps. An additional melting of the target can also result from this event. Finally, for the delay of 200 ps (Figure 11, right), the energy of the second pulse is absorbed at even longer distance from the target. Again, the shock wave originates in this region and the motion of this wave is clearly seen in the Figure. At 500 ps, a hot supercritical phase with temperature higher than 50000 K appears in the plume, and plume merging with the target liquid layer takes place. In addition, melting is observed until ≈ 1100 ps and the melted depth reaches ≈ 450 nm.

Figure 12 shows the laser ablation depth as a function of interpulse delay. The case of 0 ps delay is identical to single pulse ablation with the fluence $2 \times F_{las} = 4$ J cm^{-2}. Then, as the delay increases, the ablation depth starts to drop and, by the delay of about 30 ps, it reaches the single pulse ablation depth for F_{las}. For longer delays, the ablation depth monotonically drops below the depth of single pulse ablation, as shown in the experiments [41,57]. In fact, the plasma plume starts to expand and the second pulse reaches the target and raises the ablation crater depth. The experimentally observed linear growth of the crater depth with the number of pulses thus supports the final value of the extrapolated depth at $\Delta t \rightarrow \infty$.

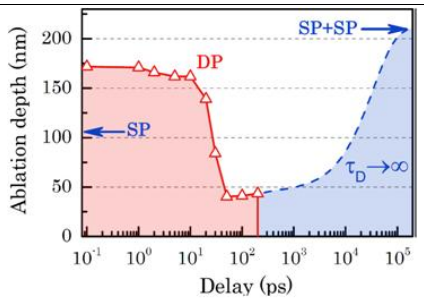

Figure 12. Ablation depth dependence on the delay between two succeeding pulses of 2 Jcm^{-2} fluence each— empty (red) triangles. The extrapolation to long delays is shown by the dashed (blue) curve. The blue arrows show the ablation depth of a single pulse of 2 J cm^{-2} fluence and two succeeding pulses with the delay $\to \infty$ [37].

Based on the above analysis, two main mechanisms could be identified to be responsible for the suppression of ablation in the DP ablation experiments [37]. The first one is associated with the suppression of the rarefaction wave, which leads to homogeneous nucleation in the liquid layer of the target under tensile stress. This mechanism dominates for the delays up to 20–50 ps and results in the monotonic decrease of the crater depth. For delays longer than 50 ps, mechanical fragmentation occurs after the first pulse, but the second pulse generates a novel high-pressured plasma region ahead of the ablated liquid layers and pushes the large fraction of these ablated layers back to the target. In this case, the ablation depth can be even smaller than that in the case of a single pulse regime.

9.5 CONCLUSIONS AND PERSPECTIVES

The given summary of experimental and theoretical investigations of material ablation with time-delayed short laser pulses reveals strong changes of the plume composition when the interpulse delay reaches the characteristic time of electron-lattice thermalization. The changes of the relative emission intensities of atoms and NPs within the plume evidence two characteristic times, suggesting thus different mechanisms responsible for the plume composition modification. It is shown that for $\Delta t \leq \tau_{el}$, the energy deposited by the second laser pulse is confined in a smaller volume due to the increased lattice temperature and the reduced electron heat conductivity. Accordingly, the atomization degree of the plume increases, in agreement with theoretical and other experimental studies. For times $\Delta t >> \tau_{el}$, the interaction of the second delayed laser pulse with the vaporized material is responsible for plasma re-heating. These observations were confirmed by ablation depth measurements and AFM analysis of the NPs collected on mica substrates.

As a consequence of the efficient reduction of the NPs fraction, and the increase of the atomic emission intensity, the performances of material analysis via DP-LIBS could be considerably improved. Understanding the complex mechanisms of DP-LA leading to the change of the sample heat regime with the interpulse delay is mandatory for the optimization of several other applications like: ultra-precise micromachining, high quality thin films synthesis by pulsed

laser deposition, and syntheses of new nanomaterials and nanostructures.

Recent theoretical studies of DP laser-metal ablation are in good agreement with experimental investigations. A further progress of laser-based applications will be possible only by a synergistic approach between numerical modeling and accurate experiments.

Indeed, developments could be foreseen in the field of laser interaction with dielectrics for applications in three-dimensional data storage, fabrication of micro- to nano-fluidic devices for single-cell analyses. Although remarkable progress was achieved in the NPs synthesis by DP-LA in liquid environments, further advances are awaited in the synthesis of new nano-objects and their direct functionalization for cancer diagnostic and treatment or for nanomedicine in general.

Finally, the simplified approach of using double pulses could open the gate for more sophisticated experiments for materials nano-processing and analyses using shaped pulses. Probing nanoscale phenomena, near-field and plasmon coupling [55] may stimulate new directions in nanoscience and nanotechnology.

Acknowledgments

E. Axente acknowledges the financial support of UEFISCDI under the PNII-RU-TE-2014-4-1790 contract.

References

1. Gao, J., Gu, H. and Xu, B. (2009). Multifunctional Magnetic Nanoparticles: Design, Synthesis, and Biomedical Applications, *Accounts Chem. Res.* **42**, pp. 1097–1107.
2. Guo, S. and Wang, E. (2011). Noble metal nanomaterials: Controllable synthesis and application in fuel cells and analytical sensors, *Nano Today* **6**, pp. 240–264.
3. De Jong, W. H. and Borm P. J. A. (2008). Drug delivery and nanoparticles: Applications and hazards, *Int. J. Nanomed.* **3**, pp. 133–149.
4. Khlebtsov, N. G. and Dykman L. A. (2010). Optical properties and biomedical applications of plasmonic nanoparticles, *J. Quant. Spectrosc. Radiat. Transf.* **111**, pp. 1–35.
5. Murphy C. J., Gole A. M., Stone J. W., Sisco P. N., Alkilany A. M., Goldsmith E. C., and Baxter S. C. (2008). Gold Nanoparticles in Biology: Beyond Toxicity to Cellular Imaging, *Accounts Chem. Res.* **41**, pp. 1721–1730.
6. Salata, O.V. (2004). Applications of nanoparticles in biology and medicine, *J. Nanobiotechnol.* **2**, pp. 1–6.
7. Wang, H., Agarwal, P., Zhao, S., Yu, J., Lu, X. and He, X. (2016). A biomimetic hybrid nanoplatform for encapsulation and precisely controlled delivery of theranostic agents, *Nat. Commun.* **6**, 10081, pp. 1–12.
8. Blanco, E., Shen, H. and Ferrari, M. (2015). Principles of nanoparticle design for overcoming biological barriers to drug delivery, *Nat. Biotechnol.* **33**, pp. 941–951.
9. Han, G., Ghosh, P., Rotello, V.M. (2007). Functionalized gold nanoparticles for drug delivery, *Nanomedicine* **2**, pp. 113–123.
10. Jiang, J., Gu, H. W., Shao, H. L., Devlin, E., Papaefthymiou, G. C., Ying, J. Y. (2008). Bifunctional Fe3O4-Ag heterodimer nanoparticles for two-photon fluorescence imaging and magnetic manipulation. *Adv. Mater.* **20**, pp. 4403–4407.

11. Xu, C. J., Xie, J., Ho, D., Wang, C., Kohler, N., Walsh, E. G., Morgan, J. R., Chin, Y. E., Sun, S. H. (2008). Au-Fe3O4 dumbbell nanoparticles as dual-functional probes. *Angew. Chem., Int. Ed.* **47**, pp. 173–176.
12. Luo, P.G. and Stutzenberger, F.J. (2008). Nanotechnology in the detection and control of microorganisms, *Adv. Appl. Microbiol.* **63**, pp. 145–81.
13. Huang, X., Jain, P.K., El-Sayed, I.H. and El-Sayed, M.A. (2008). Plasmonic photothermal therapy (PPTT) using gold nanoparticles, *Lasers. Med. Sci.* **23**, pp. 217–228.
14. Lal, S., Clare, S.E. and Halas, N.J. (2008). Nanoshell-enabled photothermal cancer therapy: impending clinical impact, *Accounts Chem. Res.* **41**, pp. 1842–1851.
15. Sun, Y. and Xia, Y. (2002). Shape-controlled synthesis of gold and silver nanoparticles, *Science* **298**, pp. 2176–2179.
16. Wang, H., Brandl, D.W., Le, F., Nordlander, P. and Halas, N.J. (2006). Nanorice: a hybrid plasmonic nanostructure, *Nano Lett.* **6**, pp. 827–832.
17. Nehl, C.L., Liao, H. and Hafner, J.H. (2006). Optical properties of star-shaped gold nanoparticles, *Nano Lett.* **6**, pp. 683–688.
18. Sun. Y, and Xia, Y. (2003). Alloying and dealloying processes involved in the preparation of metal nanoshells through a galvanic replacement reaction. *Nano Lett.* **3**, pp. 1569–1572.
19. Voloshko, A. and Itina T. E. (2015) *Nanoparticles Technology*, ed. Aliofkhazraei M., Chapter 1 "Nanoparticle Formation by Laser Ablation and by Spark Discharges — Properties, Mechanisms, and Control Possibilities" (InTech, http://dx.doi.org/10.5772/61303) pp. 1–12.
20. Caricato, A. P., Luches, A. and Martino, M. (2016) *Handbook of Nanoparticles,* ed. Aliofkhazraei M., Chapter 16 "Laser Fabrication of Nanoparticles" (Springer International Publishing Switzerland 2016) pp. 407–428.
21. Besner, S. and Meunier M. (2010). *Laser Precision Microfabrication*, eds. Sugioka, K., Meunier, M. and Piqué, A., Chapter 7 "Laser Synthesis of Nanomaterials" (Springer Series in Materials Science 135, Springer-Verlag Berlin Heidelberg) pp. 163–187.
22. Amoruso, S., Bruzzese, R., Spinelli, N., Velotta, R., Vitiello, M., Wang, X., Ausanio, G., Iannotti, V. and Lanotte, L. (2004). Generation of silicon nanoparticles via femtosecond laser ablation in vacuum, *Appl. Phys. Lett.* **84**, pp. 4502–4504.
23. Amoruso, S., Ausanio, G., Bruzzese, R., Vitiello, M. and Wang, X. (2005). Femtosecond laser pulse irradiation of solid targets as a general route to nanoparticle formation in a vacuum, *Phys. Rev. B* **71**, pp. 033406-1–033406-4.
24. Grojo, D., Hermann, J. and Perrone, A. (2005). Plasma analyses during femtosecond laser ablation of Ti, Zr, and Hf, *J. Appl. Phys.* **97**, pp. 063306-1–063306-9.
25. Hermann, J., Noël, S., Itina, T. E., Axente, E. and Povarnitsyn, M. E. (2008). Correlation between ablation efficiency and nanoparticle generation during short-pulse laser ablation of metals, *Laser Phys.* **18**, pp. 374–379.
26. Zhigilei, L. V. (2003). Dynamics of the plume formation and parameters of the ejected clusters in short-pulse laser ablation, *Appl. Phys. A-Mater. Sci. Process.* **76**, pp. 339–350.
27. Povarnitsyn, M. E., Itina, T. E., Sentis, M., Khishchenko, K. V. and Levashov, P. R. (2007). Material decomposition mechanisms in femtosecond laser interactions with metals, *Phys. Rev. B* **75**, pp. 235414-1–235414-5.
28. Povarnitsyn, M. E., Itina, T. E., Levashov, P. R. and Khishchenko, K. V. (2013). Mechanisms of nanoparticle formation by ultra-short laser ablation of metals in liquid environment, *Phys. Chem. Chem. Phys.* **15**, pp. 3108–3114.
29. Delfour, L. and Itina, T. E. (2015). Mechanisms of Ultrashort Laser-Induced Fragmentation of Metal Nanoparticles in Liquids: Numerical Insights, *J. Phys. Chem. C* **119**, pp. 13893–13900.

30. Liu, B., Hu, Z., Che, Y., Chen, Y. and Pan, X. (2007). Nanoparticle generation in ultrafast pulsed laser ablation of nickel, *Appl. Phys. Lett.* **90**, pp. 044103-1–044103-3.
31. Caricato, A. P., Luches, A. and Martino, M. (2016) *Handbook of Nanoparticles,* ed. Aliofkhazraei M., Chapter 16 "Laser Fabrication of Nanoparticles" (Springer International Publishing Switzerland 2016) pp. 407–428.
32. van de Riet, E., Nillesen, C. J. C. M. and Dieleman, J. (1993). Reduction of droplet emission and target roughening in laser ablation and deposition of metals, *J. Appl. Phys.* **74**, pp. 2008–2012.
33. Bonn, M., Denzler, D. N., Funk, S., Wolf, M., Wellershoff, S. S. and Hohlfeld, J. (2000). Ultrafast electron dynamics at metal surfaces: Competition between electron-phonon coupling and hot-electron transport, *Phys. Rev. B* **61**, pp. 1101–1105.
34. Anisimov, S. I. and Luk'yanchuk, B. S. (2002). Selected problems of laser ablation theory, *Phys. Usp.* **45**, pp. 293–324.
35. Anisimov, S. I., Kapeliovich, B. L. and Perel'man, T. L. (1974). Electron emission from metal surfaces exposed to ultrashort laser pulses, *Sov. Phys. JETP* **39**, pp. 375–377.
36. Itina, T. and Gouriet, K. (2010) *Laser Pulse Phenomena and Applications*, ed. Duarte F. J., Chapter 15 "Mechanisms of Nanoparticle Formation by Laser Ablation" (InTech, ISBN: 978-953-307-405-4) pp. 309-322.
37. Povarnitsyn, M. E., Fokin, V. B., Levashov, P. R. and Itina, T. E. (2015). Molecular dynamics simulation of subpicosecond double-pulse laser ablation of metals, *Phys. Rev. B* **92**, pp. 174104-1–174104-10.
38. Babushok, V.I., DeLucia, Jr. F.C., Gottfried, J.L., Munson, C.A. and Miziolek, A.W. (2006). Double pulse laser ablation and plasma: Laser induced breakdown spectroscopy signal enhancement, *Spectroc. Acta Pt. B-Atom. Spectr.* **61**, pp. 999–1014.
39. Beldjilali, S., Yip, W.L., Hermann, J., Baba-Hamed, T. and Belasri, A. (2011). Investigation of plasmas produced by laser ablation using single and double pulses for food analysis demonstrated by probing potato skins, *Anal. Bioanal. Chem.* **400**, pp. 2173–2183.
40. Donnelly, T., Lunney, J. G., Amoruso, S., Bruzzese, R., Wang, X., and Ni, X. (2009). Double pulse ultrafast laser ablation of nickel in vacuum, *J. Appl. Phys.* **106**, pp. 013304-1–013304-5.
41. Noël, S. and Hermann, J. (2009). Reducing nanoparticles in metal ablation plumes produced by two delayed short laser pulses, *Appl. Phys. Lett.* **94**, pp. 053120-1–053120-3.
42. Loktionov, E., Ovchinnikov, A., Protasov, Y., Protasov, Y. and Sitnikov, D. (2014). Gas-plasma flows under femtosecond laser ablation for metals in vacuum, *High Temp.* **52**, pp. 132–134.
43. Muto, H., Miyajima, K. and Mafuné, F. (2008). Mechanism of Laser-Induced Size Reduction of Gold Nanoparticles As Studied by Single and Double Laser Pulse Excitation, *J. Phys. Chem. C* **112**, pp. 5810–5815.
44. Zeng, H., Du, X., Singh, S. C., Kulinich, S. A., Yang, S., He, J. and Cai, W. (2012). Nanomaterials via Laser Ablation/Irradiation in Liquid: A Review, *Adv. Funct. Mater.* **22**, pp. 1333–1353.
45. Dell'Aglio, M., Gaudiuso, R., ElRashedy, R., De Pascale, O., Palazzo, G. and De Giacomo, A. (2013). Collinear double pulse laser ablation in water for the production of silver nanoparticles, *Phys. Chem. Chem. Phys.* **15**, pp. 20868–20875.
46. Karpukhin, V., Malikov, M., Borodina, T., Val'yano, G., Gololobova, O. and Strikanov, D. (2015). Formation of hollow micro- and nanostructures of zirconia by laser ablation of metal in liquid, *High Temp.* **53**, pp. 93–98.

47. Li, X., Zhang, G., Jiang, L., Shi, X., Zhang, K., Rong, W., Duan, J. and Lu, Y. (2015). Production rate enhancement of size-tunable silicon nanoparticles by temporally shaping femtosecond laser pulses in ethanol, *Opt. Express* **23**, pp. 4226–4232.
48. Axente, E., Mihailescu, I. N., Hermann, J. and Itina, T. E. (2011). Probing electron-phonon coupling in metals via observations of ablation plumes produced by two delayed short laser pulses, *Appl. Phys. Lett.* **99**, 081502-1–081502-3.
49. Grunwald, R., Rohloff, M., Höhm, S., Bonse, J., Krüger, J., Das, S. and Rosenfeld, A. (2011). Formation of laser-induced periodic surface structures on fused silica upon multiple cross-polarized double-femtosecond-laser-pulse irradiation sequences, *J. Appl. Phys.* **110**, pp. 014910-1–014910-4.
50. Barberoglou, M., Gray, D., Magoulakis, E., Fotakis, C., Loukakos, P. A. and Stratakis, E. (2013). Controlling ripples' periodicity using temporally delayed femtosecond laser double pulses, *Opt. Express* **21**, pp. 18501–18508.
51. Höhm, S., Rosenfeld, A., Krüger, J. and Bonse, J. (2013). Area dependence of femtosecond laser-induced periodic surface structures for varying band gap materials after double pulse excitation, *Appl. Surf. Sci.* **278**, pp. 7–12.
52. Derrien, T. J.-Y., Krüger, J., Itina, T. E., Höhm, S., Rosenfeld, A. and Bonse, J. (2014). Rippled area formed by surface plasmon polaritons upon femtosecond laser double-pulse irradiation of silicon: the role of carrier generation and relaxation processes, *Appl. Phys. A-Mater. Sci. Process.* **117**, pp. 77–81.
53. Povarnitsyn, M. E., Itina, T. E., Khishchenko, K.V. and Levashov, P. R. (2009). Suppression of Ablation in Femtosecond Double-Pulse Experiments, *Phys. Rev. Lett.* **103**, pp. 195002-1–195002-4.
54. Roth, J., Krauß, A., Lotze, J. and Trebin, H.-R. (2014). Simulation of laser ablation in aluminum: the effectivity of double pulses, *Appl. Phys. A-Mater. Sci. Process.* **117**, pp. 2207–2216.
55. Stoian, R., Wollenhaupt, M., Baumert, T. and Hertel, I. V. (2010) *Laser Precision Microfabrication*, eds. Sugioka, K., Meunier, M. and Piqué, A., Chapter 5 "Temporal Pulse Tailoring in Ultrafast Laser Manufacturing Technologies" (Springer Series in Materials Science 135, Springer-Verlag Berlin Heidelberg) pp. 121–144.
56. Gautier, C., Fichet, P., Menut, D., Lacour, J.-L., L'Hermite, D. and Dubessy, J. (2004). Study of the double-pulse setup with an orthogonal beam geometry for laser-induced breakdown spectroscopy, *Spectroc. Acta Pt. B-Atom. Spectr.* **59**, pp. 975–986.
57. Semerok, A. and Dutouquet, C. (2004). Ultrashort double pulse laser ablation of metals, *Thin Solid Films* **453–454**, pp. 501–505.
58. Fortes, F. J., Moros, J., Lucena, P., Cabalin, L. M. and Laserna, J. J. (2013). Laser-Induced Breakdown Spectroscopy, *Anal. Chem.* **85**, pp. 640–669.
59. Piscitelli, V., Martínez, M. A., Fernandez, A. J., Gonzalez J. J., Mao X. L. and Russo, R. E. (2009). Double pulse laser induced breakdown spectroscopy: Experimental study of lead emission intensity dependence on the wavelengths and sample matrix *Spectroc. Acta Pt. B-Atom. Spectr.* **64**, pp. 147−154.
60. Gautier, C., Fichet, P., Menut, D., Lacour, J.-L., L'Hermite, D. and Dubessy, J. (2005). Quantification of the intensity enhancements for the double-pulse laser-induced breakdown spectroscopy in the orthogonal beam geometry, *Spectroc. Acta Pt. B-Atom. Spectr.* **60**, pp. 265–276.
61. Sasaki, A., Liu, J., Hara, W., Akiba, S., Saito, K., Yodo, T. and Yoshimoto, M. (2004). Room-temperature growth of ultrasmooth AlN epitaxial thin films on sapphire with NiO buffer layer, *J. Mat. Research* **19**, pp. 2725–2729.
62. Bruneau, S., Hermann, J., Dumitru, G., Sentis, M. and Axente, E. (2005). Ultra-fast laser ablation applied to deep-drilling of metals, *Appl. Surf. Sci.* **248**, pp. 299–303.

63. Chimier, B., Tikhonchuk, V. T. and Hallo, L. (2007). Heating model for metals irradiated by a subpicosecond laser pulse, *Phys. Rev. B* **75**, pp. 195124-1–195124-12.
64. Noël, S., Hermann, J. and Itina, T. E. (2007). Investigation of nanoparticle generation during femtosecond laser ablation of metals, *Appl. Surf. Sci.* **253**, pp. 6310–6315.
65. Ganeev, R. A., Hutchison, C., Lopez-Quintas, I., McGrath, F., Lei, D.Y., Castillejo, M. and Marangos, J. P. (2013). Ablation of nanoparticles and efficient harmonic generation using a 1-kHz laser, *Phys. Rev. A* **88**, pp. 033803-1–033803-10.
66. Starikov, S. V. and Pisarev, V. V. (2015). Atomistic simulation of laser-pulse surface modification: Predictions of models with various length and time scales, *J. Appl. Phys.* **117**, pp. 135901-1–135901-9.
67. Wu, C., Christensen, M. S., Savolainen, J.-M., Balling, P. and Zhigilei, L. V. (2015). Generation of subsurface voids and a nanocrystalline surface layer in femtosecond laser irradiation of a single-crystal Ag target, *Phys. Rev. B* **91**, pp. 035413-1–035413-14.
68. Cheng, C. and Xu, X. (2005). Mechanisms of decomposition of metal during femtosecond laser ablation, *Phys. Rev. B* **72**, pp. 165415-1–165415-15.
69. Chimier, B., Tikhonchuk, V. T. and Hallo, L. (2008). Effect of pressure relaxation during the laser heating and electron–ion relaxation stages, *Appl. Phys. A-Mater. Sci. Process.* **92**, pp. 843–848.
70. Miotello, A. and Kelly, R. (1995). Critical assessment of thermal models for laser sputtering at high fluencies, *Appl. Phys. Lett.* **67**, pp. 3535-1–3535-3.
71. Colombier, J. P., Combis, P., Bonneau, F., Le Harzic, R. and Audouard, E. (2005). Hydrodynamic simulations of metal ablation by femtosecond laser irradiation, *Phys. Rev. B* **71**, pp. 165406-1–165406-6.
72. Perez, D. and Lewis, L. (2002). Ablation of solids under femtosecond laser pulses, *Phys. Rev. Lett.* **89**, pp. 255504-1–255504-4.
73. Norman, G. E., Starikov, S. V. and Stegailov, V. V. (2012). Atomistic simulation of laser ablation of gold: Effect of pressure relaxation, *Sov. Phys. JETP* **114**, pp. 792–800.
74. Nolte, S., Momma, C., Jacobs, H., Tünnermann, A., Chichkov, B. N., Wellegehausen, B. and Welling, H. (1997). Ablation of metals by ultrashort laser pulses, *J. Opt. Soc. Am. B* **14**, pp. 2716–2722.
75. Furusawa K., Takahashi K., Kumagai H., Midorikawa, K. and Obara M. (1999). Ablation characteristics of Au, Ag, and Cu metals using a femtosecond Ti:sapphire laser, *Appl. Phys. A-Mater. Sci. Process.* **69**, pp. S359–S366.
76. Hirayama, Y. and Obara, M. (2002). Heat effects of metals ablated with femtosecond laser pulses, *Appl. Surf. Sci.* **197–198**, pp. 741–745.
77. Axente, E., Noël, S., Hermann, J., Sentis, M. and Mihailescu, I. N. (2009). Subpicosecond laser ablation of copper and fused silica: Initiation threshold and plasma expansion, *Appl. Surf. Sci.* **255**, pp. 9734–9737.
78. Hermann, J., Mercadier, L., Axente, E. and Noël, S. (2012). Properties of plasmas produced by short double pulse laser ablation of metals, *J. Phys.: Conf. Ser.* **399**, pp. 012006-1–012006-12.
79. Hohlfeld, J., Wellershoff, S. S., Grüdde, J., Conrad, U., Jänke, V. and Matthias, E. (2000). Electron and lattice dynamics following optical excitation of metals, *Chem. Phys.* **251**, pp. 237–258.
80. Schäfer, C., Urbassek, H. M. and Zighilei, L. V. (2002). Metal ablation by picosecond laser pulses: A hybrid simulation, *Phys. Rev. B* **66**, pp. 115404-1–115404-8.
81. Kanavin, A., Smetanin, I., Isakov, V., Afanasiev, Y., Chichkov, B., Wellegehausen, B., Nolte, S., Momma, C. and Tünnermann, A. (1998). Heat transport in metals irradiated by ultrashort laser pulses, *Phys. Rev. B* **57**, pp. 14698-14703.

82. Scuderi, D., Albert, O., Moreau, D., Pronko, P. P. and Etchepare, J. (2005). Interaction of a laser-produced plume with a second time delayed femtosecond pulse, *Appl. Phys. Lett.* **86**, pp. 071502-1–071502-3.
83. Noël, S. and Hermann, J. (2007). Influence of irradiation conditions on plume expansion induced by femtosecond laser ablation of gold and copper, *Proc. SPIE, ROMOPTO 2006: Eighth Conference on Optics* **6785**, *67850F*.
84. Le Harzic, R., Breitling, D., Sommer, S., Föhl, C., König, K., Dausinger, F. and Audouard, E. (2005). Processing of metals by double pulses with short laser pulses, *Appl. Phys. A-Mater. Sci. Process.* **81**, pp. 1121–1125.
85. Spyridaki, M., Koudoumas, E., Tzanetakis, P., Fotakis, C., Stoian, R., Rosenfeld, A. and Hertel, I. V. (2003). Temporal pulse manipulation and ion generation in ultrafast laser ablation of silicon, *Appl. Phys. Lett.* **83**, pp. 1474–1476.
86. Stoian, R., Boyle, M., Thoss, A., Rosenfeld, A., Korn, G., Hertel, I. V. and Campbell, E. E. B. (2002). Laser ablation of dielectrics with temporally shaped femtosecond pulses, *Appl. Phys. Lett.* **80**, pp. 353–355.
87. Guarnaccio, A., Parisi, G.P., Mollica, D., De Bonis, A., Teghil, R. and Santagata, A. (2014). Fs–ns double-pulse Laser Induced Breakdown Spectroscopy of copper-based-alloys: Generation and elemental analysis of nanoparticles, *Spectroc. Acta Pt. B-Atom. Spectr.* **101**, pp. 261–268.
88. Garrelie, F., Bourquard, F., Loir, A.–S., Donnet, C. and Colombier J.-P. (2016). Control of femtosecond pulsed laser ablation and deposition by temporal pulse shaping, *Opt. Laser Technol.* **78**, pp. 24–51.
89. Wang, Q., Luo, S., Chen, Z., Qi, H., Deng, J. and Hu, Z. (2016). Drilling of aluminum and copper films with femtosecond double-pulse laser, *Opt. Laser Technol.* **80**, pp. 116–124.
90. Chowdhury, I. H., Xu, X. and Weiner, A. M. (2005). Ultrafast double-pulse ablation of fused silica, *Appl. Phys. Lett.* **86**, pp. 151110-1–151110-3.
91. Deng, Y. P., Xie, X. H., Xiong, H., Leng, Y. X., Cheng, C. F., Lu, H. H., Li, R. X. and Xu, Z. Z. (2005). Optical breakdown for silica and silicon with double femtosecond laser pulses, *Opt. Express* **13**, pp. 3096–3103.
92. Hu, Z., Singha, S., Liu, Y. and Gordon, R. J. (2007). Mechanism for the ablation of Si<111> with pairs of ultrashort laser pulses, *Appl. Phys. Lett.* **90**, pp. 131910-1–131910-3.
93. Schiffern, J. T., Doerr, D. W. and Alexander, D. R. (2007). Optimization of collinear double-pulse femtosecond laser-induced breakdown spectroscopy of silicon, *Spectroc. Acta Pt. B-Atom. Spectr.* **62**, pp. 1412–1418.
94. Amendola, V. and Meneghetti, M. (2013). What controls the composition and the structure of nanomaterials generated by laser ablation in liquid solution?, *Phys. Chem. Chem. Phys.* **15**, pp. 3027–3046.
95. De Giacomo, A., Dell'Aglio, M., Santagata, A., Gaudiuso, R., De Pascale, O., Wagener, P., Messina, G. C., Compagnini, G. and Barcikowski, S. (2013). Cavitation dynamics of laser ablation of bulk and wire-shaped metals in water during nanoparticles production, *Phys. Chem. Chem. Phys.* **15**, pp. 3083–3092.
96. Besner, S., Kabashin, A. V. and Meunier, M. (2006). Fragmentation of colloidal nanoparticles by femtosecond laser-induced supercontinuum generation, *Appl. Phys. Lett.* **89**, pp. 233122-1–233122-3.
97. Stratakis, E., Barberoglou, M., Fotakis, C., Viau, G., Garcia, C. and Shafeev, G. A. (2009). Generation of Al nanoparticles via ablation of bulk Al in liquids with short laser pulses, *Opt. Express* **17**, pp. 12650–12659.

98. Besner, S. and Meunier M. (2010) *Laser Precision Microfabrication*, eds. Sugioka, K., Meunier, M. and Piqué, A., Chapter 7 "Laser Synthesis of Nanomaterials" (Springer Series in Materials Science 135, Springer-Verlag Berlin Heidelberg) pp. 163-187.
99. Burakov, V. S., Tarasenko, N. V., Butsen, A. V., Rotzantsev, V. A. and Nedel'ko, M. I. (2005). Formation of nanoparticles during double-pulse laser ablation of metals in liquids, *Eur. Phys. J.: Appl. Phys.* **30**, pp. 107–112.
100. Phuoc, T. X., Soong, Y. and Chyu, M. K. (2007). Synthesis of Ag-deionized water nanofluids using multi-beam laser ablation in liquids, *Opt. Lasers Eng.* **45**, pp. 1099–1106.
101. Burakov, V. S., Butsen, A. V. and Tarasenko, N. V. (2010). Laser-induced plasmas in liquids for nanoparticle synthesis, *J. Appl. Spectrosc.* **77**, pp. 386–393.
102. Casavola, A., De Giacomo, A., Dell'Aglio, M., Taccogna, F., Colonna, G., De Pascale, O. and Longo, S. (2005). Experimental investigation and modelling of double pulse laser induced plasma spectroscopy under water, *Spectroc. Acta Pt. B-Atom. Spectr.* **60**, pp. 975–985.
103. Caminat, P., Valerio, E., Autric, M., Grigorescu, C. and Monnereau, O. (2004). Double beam pulse laser deposition of NiMnSb thin films at ambient temperature, *Thin Solid Films* **453–454**, pp. 269–272.
104. György, E., Santiso, J., Giannoudakos, A., Kompitsas, M., Mihailescu, I.N. and Pantelica, D. (2005). Growth of Al doped ZnO thin films by a synchronized two laser system, *Appl. Surf. Sci.* **248**, pp. 147–150.
105. György, E., Sauthier, G., Figueras, A., Giannoudakos, A., Kompitsas, M. and Mihailescu, I.N. (2006). Growth of Au–TiO2 nanocomposite thin films by a dual-laser, dual-target system, *J. Appl. Phys.* **100**, pp. 114302-1–114302-5.
106. Kompitsas, M., Giannoudakos, A., György, E., Sauthier, G., Figueras, A. and Mihailescu, I.N. (2007). Growth of metal-oxide semiconductor nanocomposite thin films by a dual-laser, dual target deposition system, *Thin Solid Films* **515**, pp. 8582–8585.
107. Fasaki, I., Kandyla, M., Tsoutsouva, M.G. and Kompitsas, M. (2013). Optimized hydrogen sensing properties of nanocomposite NiO:Au thin films grown by dual pulsed laser deposition, *Sens. Actuator B-Chem.* **176**, pp. 103–109.
108. Kuzyakov, Yu. Ya., Varakin, V. N., Moskvitina, E. N. and Stolyarov, P. M. (2009). Double-pulse laser ablation applied to reactive PLD method for synthesis of carbon nitride film: A second laser shot delay, *Laser Phys.* **19**, pp. 1159–1164.
109. György, E., Mihailescu, I.N., Kompitsas, M. and Giannoudakos A. (2002). Particulates-free Ta thin films obtained by pulsed laser deposition: the role of a second laser in the laser-induced plasma heating, *Appl. Surf. Sci.* 195, pp. 270–276.
110. Gusarov, A. V. and Smurov, I. (2005). Thermal model of nanosecond pulsed laser ablation: analysis of energy and mass transfer, *J. Appl. Phys.* **97**, pp. 014307-1–014307-13.
111. Anisimov, S. I., Bonch-Brouevich, A. M., El'yashevich, M. A., Imas, Ya. A., Pavlenko, N. A. and Romanov, G. S. (1967). Effect of powerful light fluxes on metals, *Sov. J. Tech. Phys.* **11**, pp. 945–952.
112. Olstad, R. A. and Olander, D. R. (1975). Evaporation of solids by laser pulses. I. Iron, *J. Appl. Phys.* **46**, pp. 1499–1508.
113. Garrison, B. J., Itina, T. E. and Zhigilei, L. V. (2003). Limit of overheating and the threshold behavior in laser ablation, *Phys. Rev. E* **68**, pp. 041501-1–041501-4.
114. Martynyuk, M. M. (1974). Vaporization and boiling of liquid metal in an exploding wire, *Sov. Phys. Thech. Phys.* **19**, pp. 793–797.
115. Martynyuk, M. M. (1983). Critical constants of metals, *Russ. J. Phys. Chem.* **57**, pp. 494–501.

116. Luk'yanchuk B., Bityrin N., Anisimov S., Malyshev A., Arnold N. and Bäuerle, D. (1996). Photophysical ablation of organic polymers: the influence of stresses, *Appl. Surf. Sci.* **106**, pp. 120-125.
117. Nolte, S., Chichkov, B. N., Welling, H., Shani, Y., Lieberman, K. and Terkel, H. (1999). Nanostructuring with spatially localized femtosecond laser pulses, *Opt. Lett.* **24**, pp. 914–916.
118. Amoruso, S., Bruzzese, R., Vitiello, M., Nediakov, N. N., and Atanasov, P. A. (2005). Experimental and theoretical investigations of femtosecond laser ablation of aluminum in vacuum, *J. Appl. Phys.* **98**, pp. 044907-1–044907-7.
119. Plech, A., Kotaidis, V., Lorenc, M. and Boneberg, J. (2006). Femtosecond laser near-field ablation from gold nanoparticles, *Nat. Phys.* **2**, pp. 44–47.
120. Komashko, A. M., Feit, M. D., Rubenchik, A. M., Perry, M. D. and Banks, P. S. (1999). Simulation of material removal efficiency with ultrashort laser pulses, *Appl. Phys. A-Mater. Sci. Process.* **69**, pp. S95–S98.
121. Rethfeld, B., Sokolowski-Tinten, K., von der Linde, D. and Anisimov, S. I. (2002). Ultrafast thermal melting of laser-excited solids by homogeneous nucleation, *Phys. Rev. B* **65**, pp. 092103-1–092103-4.
122. Ivanov, D. S. and Zhigilei, L. V. (2003). Combined atomistic-continuum modeling of short-pulse laser melting and disintegration of metal films, *Phys. Rev. B* **68**, pp. 064114-1 - 064114-22.
123. Eidmann, K., Meyer-ter-Vehn, J., Schlegel, T. and Hüller, S. (2000). Hydrodynamic simulation of subpicosecond laser interaction with solid-density matter, *Phys. Rev. E* **62**, pp. 1202–1214.
124. Vidal, F., Johnston, T. W., Laville, S., Barthélemy, O., Chaker, M., Le Drogoff, B., Margot, J. and Sabasi, M. (2001). Critical-Point Phase Separation in Laser Ablation of Conductors, *Phys. Rev. Lett.* **86**, pp. 2573–2576.
125. Glover, T. E. (2003). Hydrodynamics of particle formation following femtosecond laser ablation, *J. Opt. Soc. Am. B* **20**, pp. 125–131.
126. Zhigilei, L. V. and Garrison, B. J. (2000). Microscopic mechanisms of laser ablation of organic solids in the thermal and stress confinement irradiation regimes, *J. Appl. Phys.* **88**, pp. 1281–1298.
127. Perez, D. and Lewis, L. J. (2003). Molecular-dynamics study of ablation of solids under femtosecond laser pulses, *Phys. Rev. B* **67**, pp. 184102-1–184102-15.
128. Itina, T. E., Vidal, F., Delaporte, P., Sentis, M. (2004). Numerical study of ultra-short laser ablation of metals and of laser plume dynamics, *Appl. Phys. A* **79**, pp. 1089–1092.
129. Miller, G. H. and Puckett, E. G. (1996). A high-order godunov method for multiple condensed phases, *J. Comput. Phys.* **128**, pp. 134–164.
130. Povarnitsyn, M. E., Itina, T. E., Khishchenko, K. V. and Levashov, P. R. (2007). Multi-material two-temperature model for simulation of ultra-short laser ablation, *Appl. Surf. Sci.* **253**, pp. 6343–6346.
131. Khishchenko, K. V., in Physics of Extreme States of Matter—2005 (IPCP RAS, Chernogolovka, 2005), pp. 170–172.
132. Frenkel, J., Kinetic Theory of Liquids (Clarendon Press, Oxford, 1946).
133. Grady D. E. (1988). The spall strength of condensed matter, *J. Mech. Phys. Solids* **36**, pp. 353–384.
134. Born, M., Wolf, E., Principles of optics: electromagnetic theory of propagation, interference and diffraction of light (Pergamon Press, Oxford, 1964).
135. Zhakhovskii V., Inogamov N., Petrov Y., Ashitkov S. and Nishihara K. (2009). Molecular dynamics simulation of femtosecond ablation and spallation with different interatomic potentials, *Appl. Surf. Sci.* **255**, pp. 9592–9596.